

# Boundary curvature-dependent dynamical trapping of undulating worms

Sohum Kapadia and Arshad Kudrolli

*Department of Physics, Clark University, Worcester, MA 01610*

(Dated: January 22, 2025)

We investigate the behavior of *Lumbriculus variegatus* in polygonal chambers and show that the worms align with the boundaries as they move forward and get dynamically trapped at concave corners over prolonged periods of time before escaping. We develop a kinematic model to calculate and describe the evolution of the worm's mean body orientation angle relative to the boundary. Performing simulations with a minimal active elastic dumbbell model, we then show that both the boundary aligning and corner trapping behavior of the worm are captured by steric interactions with the boundaries. The dimensionless ratio of the strength of forward motion and diffusion caused by the worm's undulatory and peristaltic strokes is shown to determine the boundary alignment dynamics and trapping time scales of the worm. The simulations show that the body angle with the boundary while entering the concave corner is important to the trapping time distributions with shallow angles leading to faster escapes. Our study demonstrates that directed motion and limited angular diffusion can give rise to aggregation which can mimic shelter seeking behavior in slender undulating limbless worms even when thigmotaxis or contact seeking behavior is absent.

## I. INTRODUCTION

Boundary following and corner aggregation are observed widely in active matter ranging from motile cells to multicellular organisms and play an important role in nature. For instance, sperms rely on the boundary to move up the tortuous reproductive tract to fertilize the egg [1–3]. Thigmotaxis, or contact seeking behavior is known to occur in large animals such as flies, rats, cockroaches, fish, and humans as they search shelter and navigate disordered environments [4–11]. At large scale, it has been demonstrated that a collection of mechanical robots show boundary following and corner aggregation as in infant rats confined to rectangular enclosures [6]. Oblong polar active matter can be prevented from rotating by the presence of others due to steric interactions and can consequently get trapped at boundaries [12]. At smaller scales, *E. coli* are known to accumulate and align parallel to surfaces [13–15]. Differences in physiology and locomotion strategies means that while the observed phenomena may appear the same, the mechanisms which give rise to them may differ considerably.

Viscous forces dominate and inertia is negligible in micron-sized sperm and bacteria, and thus they experience long range hydrodynamic interactions with a boundary which can lead to alignment [16]. Nonetheless, studies also explain the boundary aligning behavior of micro-swimmers based on interactions due to direct ciliary contact interactions that induce torques on the body of the organism leading to change in their relative orientation with a surface [13, 17]. Active particles have been shown with simulations to slide across long distances along obstacles using topotaxis [18, 19]. However, clear examples using full body tracking with actual organisms that illustrate the exact mechanism at play are limited. Few studies have been conducted where the phenomena has been thoroughly studied from a physical perspective when the interactions with boundaries are limited to the sense of touch, as opposed to phototaxis, chemotaxis, and geotaxis [20, 21]. Such a regime can be experienced even by humans as for example in total darkness [22].

*Lumbriculus variegatus*, also known as the California blackworm or blackworm, belonging to the Oligochaeta subclass of the Annelida phylum are found widely in the sediments at the bottom of shallow fresh water bodies. *L. variegatus*, along with *T. tubifex*, have become an important model to study active matter in the laboratory [23–34]. These centimeter-scale slender worms typically move in water and soft sediments with transverse undulatory and peristaltic strokes [29], but can disperse rapidly over short distances with helical strokes or body reversals when threatened [27, 31], and show a rich set of behavior including forming blobs that can adaptively move around in response to external stimuli such as temperature, light and physical stresses [32, 34–36]. Recently it was shown that *L. variegatus* use their prostomial nerves to probe physical obstacles and follow the boundary while moving in a circular chamber even while occasionally switching directions [30]. Whether thigmotaxis was important to the observed behavior could not be ascertained since the boundary curvature was constant and positive. Thus, the mechanism by which *L. variegatus* end up at the boundaries remained unclear.

Here, we examine the spatial distribution of a single blackworm when it is confined to water filled chambers with concave and convex corners. Transparent chambers are constructed that enable full body tracking of the aquatic worm to investigate the role of boundary curvature on their behavior near impenetrable boundaries. Our observations show that the worm progressively aligns with the boundary as it comes in contact before getting trapped in a concave corner of the chamber. Whereas, we find that the worms simply continue on into the chamber, and do not follow the boundary, at a convex corner. Utilizing a square chamber, we investigate the travel distance over which the worm

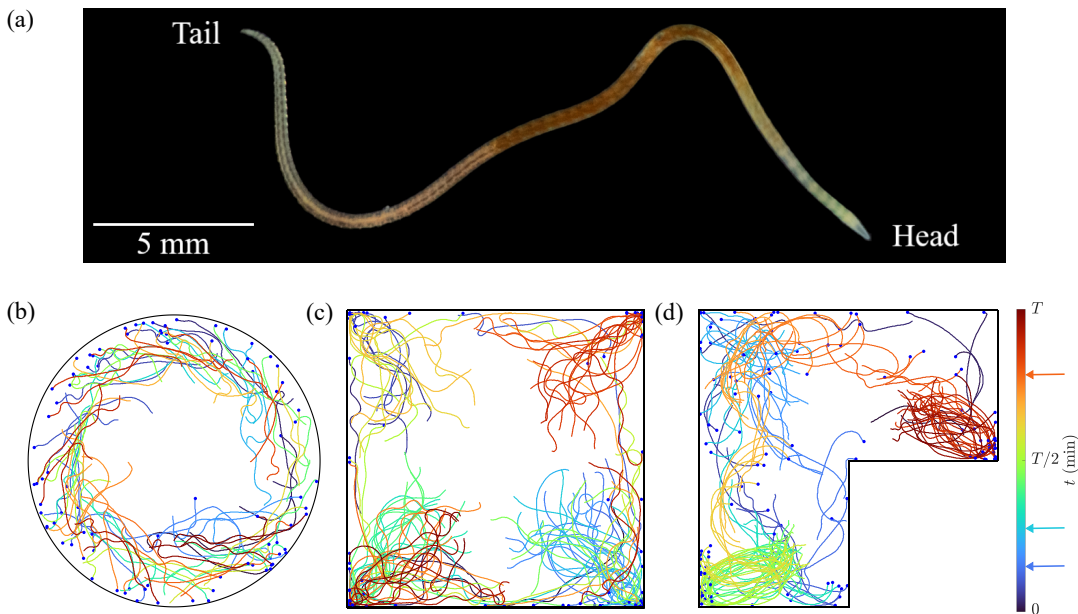


FIG. 1. (a) An image of *Lumbriculus variegatus*, aka California blackworm studied. (b-d) Superposed snapshots of the worm at  $\Delta t = 10$  seconds time intervals moving inside a circular chamber with diameter  $d = 4$  cm (b), a square chamber with side length  $l = 4$  cm (c), and a polygon chamber with long sides  $l = 4$  cm (d), over total observation time  $T = 18$  min, 21 min, and 25 min, respectively. The snapshots correspond to time  $t$  denoted by the color map. The location of the head is indicated by a solid blue marker and is observed to stay close to the boundary in the circular chamber, and predominantly near the concave corners in the square chamber. The head remains close to the concave corner and does not follow the boundary around the convex corner in the polygonal chamber.

orients itself with the boundary, and the time scales over which gets trapped at corners and the time taken to travel between corners. These observations enable us to quantitatively investigate the physical mechanisms which determine the observed localization behavior with complementary simulations using a bead-spring model. Our simulations reproduce many salient observed features showing that boundary following and localization at corners can arise due to purely dynamical reasons in such long slender organisms that interact with a boundary only during contact.

## II. BOUNDARY ALIGNMENT AND CORNER LOCALIZATION

An image of a California blackworm used in our study is shown in Fig. 1(a). A worm with length  $l_w$  between 20 mm and 30 mm is picked at random from a reservoir and placed in a quasi-two dimensional observation chamber constructed by laser-cutting holes in clear acrylic sheets, and sandwiching them flat between clear acrylic sheets in a larger water-filled container. The thickness of the resulting chamber  $h = 1.5$  mm is chosen so that it is much larger than the worm thickness which is about a tenth of a millimeter following previous practice [30]. Further information on the imaging and full body shape tracking techniques can be found in the Supplementary Information (SI) [37].

Figure 1(b-d) shows three representative chambers with increasingly complex shapes used in our investigations along with a snapshot of the worm, illustrating the typical dynamics observed within them over a time interval  $T$ .

In the circular chamber shown in Fig. 1(b) and Movie S1, we observe that the worm can be found essentially following the boundary with the head close to the boundaries. Over long periods, the worm is observed to move clockwise and anticlockwise while occasionally switching directions consistent with previous observations [30].

In a square chamber shown in Fig. 1(c) and Movie S2, we observe by contrast that the worm can be found not only near the boundaries, but also appears to be trapped at the concave corners over prolonged periods of time before moving to a neighboring corner. When we further examine the worm in a polygonal chamber with a convex corner with internal angle  $\frac{3\pi}{2}$ , the worm is observed to stay for extended periods at one of the concave corners, besides moving along the boundary or across the chamber (see Fig. 1(d) and Movie S3).

While the worm is observed to approach the convex corner, it neither stays there as in the case of the concave corners, nor does it round the corner to continue along the boundary. Rather, it is found to just continue on into the central portion of the chamber before encountering a side boundary and getting trapped at a concave corner as in the square chamber. Further, one can observe examples where the worm moves away from the boundary approximately

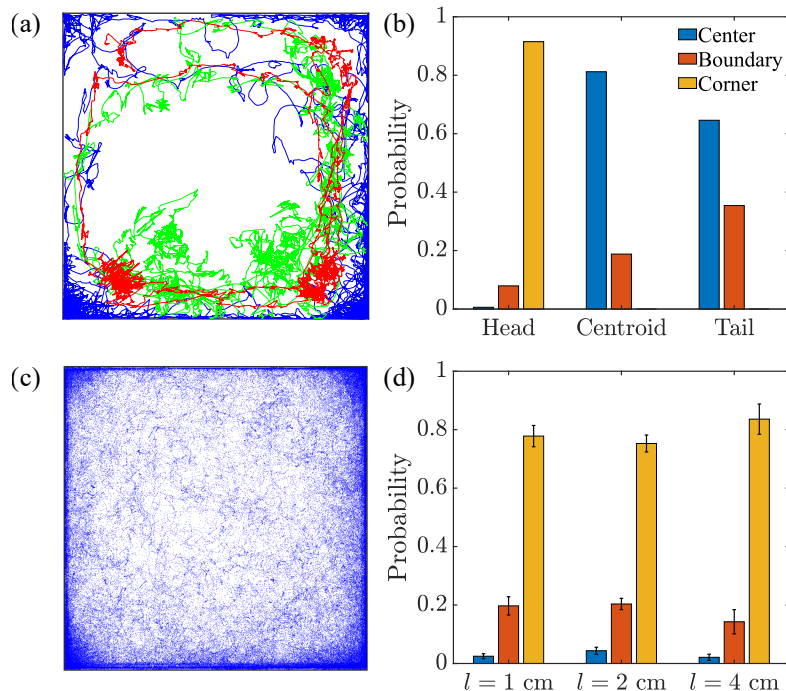


FIG. 2. (a) The trajectory of the head (blue), centroid (red), and tail (green) of a California blackworm moving in a square chamber ( $l = 4$  cm). The worm coordinates are shown at  $\Delta t = 42$  ms time intervals over  $T = 10$  minutes. (b) The corresponding probability of finding the head, centroid, and tail in various parts of the chamber shows the localization of the head near the corners. (c) The head position (blue dot markers) observed over 10 trials lasting  $T = 30$  minutes each shows that the worm occasionally moves into the central regions of the chamber. (d) The probability of finding the head in square chambers with  $l = 10$  mm, 20 mm and 40 mm all show localization of the head at the corners ( $l_w = 25 \pm 5$  mm). The error bars denote root mean square deviations of a trial from the mean.

at time  $t = 4$  min, 7 min and 19 min that are indicated by arrows in the color bar.

The observations that the worm do not bend around the convex corner while moving along the boundary in convex polygonal chambers, and the spontaneous departures from the flat boundaries implies that the worm do not show an attraction to the boundary. The fact that the worms often leave the relative shelter of the boundaries also suggests that thigmotaxis is not the reason for why the worm is found near the boundary as they move about the chamber, but rather suggests a dynamical mechanism for the aggregation behavior. In the following, we focus on the square chamber to develop a quantitative understanding of the worm interactions with a flat boundary and localization at the concave corners.

### III. OBSERVATIONS

#### A. Spatial distribution of the worm

The tracked positions of the head, tail, and centroid of a worm of length  $l_w = 23$  mm in the square chamber with side length  $l = 4$  cm is plotted in Fig. 2(a) as it moves nearly twice around the chamber while visiting the corners. It is evident that the head stays closer to boundary while the tail stays further away from the boundary, consistent with the example shown in Fig. 1(b). One can also see similarities and differences in comparing with its trajectory in the circular chamber shown in Fig. 1(a). While the overall relative orientation of the head w.r.t. the boundary is similar, we observe that the distance of the centroid from the boundaries varies systematically as the worm moves along the boundary (see SI [37]). This is in contrast with the trajectory of the worm in circular chambers, where its centroid moves around more or less in a circle, some distance away from the boundary, while its body undulates and maintains a more or less constant angle with respect to the normal.

These measurements indicate the worm's head is relatively pinned when it is in the corner, and the interaction with the boundaries has a quantitative effect on the worm's strokes. We divide the spatial position of the worm in

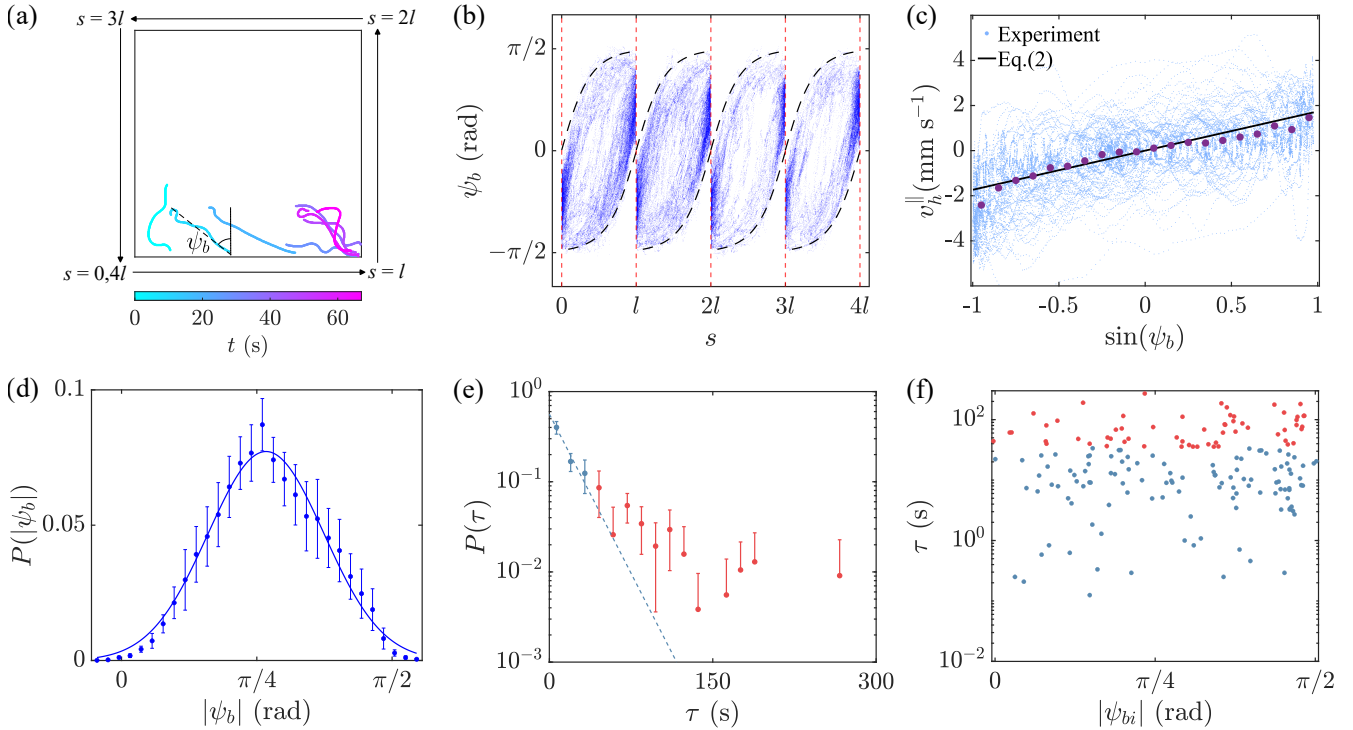


FIG. 3. (a) Snapshots of a worm as it aligns with a boundary and gets trapped in a corner. The time corresponds to the color map. (b) A scatter plot of body orientation  $\psi_b$  versus distance along perimeter  $s$ . The dashed (black) lines correspond to Eq. (4) calculated with the kinematic model, and the vertical dotted (red) lines correspond to the worms trapped at the corners. (c) The scatter plot of  $v_h^{\parallel}$  as a function of  $\sin \psi_b$  each time a worm contacts a boundary. A linear fit (solid black line) using Eq. (1) with  $v_h = 1.74 \text{ mm s}^{-1}$  is observed to be in agreement with the observed means shown with circle markers. (d) The probability distribution function (PDF) of  $|\psi_b|$  while the worm is in the corner ( $l = 40 \text{ mm}$ ;  $n_T = 10$  trails;  $T = 30$  minutes each). A Gaussian distribution with mean  $0.84 \text{ rad}$  and standard deviation  $\sigma = 0.34 \text{ rad}$  is also plotted for reference. (e) The probability distribution of trap time  $\tau$  at a corner. An exponential function fit with a mean  $\langle \tau \rangle = 22 \text{ s}$  is also shown (line). (f) The measured  $\tau$  plotted versus initial orientation angle  $|\psi_{ci}|$  of the worm as it enters the corner is scattered over a wide range.

the chamber into three regions to quantify their distribution. The corner regions correspond to distances less than  $r_c = 3 \text{ mm}$  from each corner. The boundary regions correspond to distances that are less than  $r_b = \frac{r_c}{\sqrt{2}}$  from any side boundaries, excluding those which belong to the corner regions. The central region with sides  $l - 2r_b$  correspond to the remaining locations that are more than  $r_b = \frac{r_c}{\sqrt{2}}$  from any side boundaries and thus do not belong to either corner or boundary regions. The distances  $r_c$  and  $r_b$  are chosen so that short stroke duration related departures from the boundaries are still labeled as belonging to the corner or boundary regions. Measuring the root mean square fluctuation of the head and centroid, we find them to be  $\sqrt{\langle \Delta r_h^2 \rangle} = 5.74 \pm 0.74 \text{ mm}$ ,  $\sqrt{\langle \Delta r_c^2 \rangle} = 2.64 \pm 0.63 \text{ mm}$  while near the chamber center and  $\sqrt{\langle \Delta r_h^2 \rangle} = 1.14 \pm 0.07 \text{ mm}$  and  $\sqrt{\langle \Delta r_c^2 \rangle} = 1.36 \pm 0.20 \text{ mm}$  while near a corner, consistent with our choice of  $r_c$ .

We plot the probability of the head, the centroid and the tail in the different regions accounting for the differences in area in Fig. 2(b). We observe that the head is found in one of the corners over 88% of the time in this case, whereas, the tail and the centroid are never found in the corner, and are more typically found in the central or boundary regions. In Fig. 2(c), we further plot the position of the head over a large data set consisting of 10 trials lasting 30 minutes tracked with the camera at 24 frames per second. Figure 2(d) shows the probability corresponding to not only this larger data set, but also for those from chambers with  $l = 10 \text{ mm}$  and  $20 \text{ mm}$ . The worm's head is found mostly at the corners in all three cases, showing the robustness of the localization.

## B. Boundary aligning dynamics of the worm

Figure 3(a) shows sample snapshots of a worm moving near a boundary, where the distance  $s$  is measured counterclockwise along the perimeter of the chamber from the bottom left vertex. The behavior of the worm when it

encounters the boundary is quantified by the angle  $\psi_b$  that the line joining the head and the centroid of the worm makes with the normal to the boundary. One can observe that the worm increasingly aligns with the boundary, and is then found oriented along the angle bisector, while touching the boundaries on both sides of the corner as it continues to undulate and perform peristaltic strokes while trapped at the corner.

The observed interactions in the square chamber is different from that observed in the circular chamber. In the circular chamber, the worm is observed to follow the boundary clockwise and counterclockwise with its body orientation w.r.t. the normal to the boundary peaked around  $\psi_b \approx 1.15$  rad. Thus, the average rate with which the worm's body changes direction due to collisions with the boundary match the change in the normal to the boundary as the worm moves along it. In a previous study with *L. variegatus* in circular chambers with a smaller radius it was observed  $\psi_b$  was centered about a lower angle 0.56 rad [30]. This would imply that near a flat boundary, the angle which the worm makes with the boundary normal would evolve as the worm moves forward and approach  $\pi/2$  rad or  $-\pi/2$  rad. Indeed, this is what we observe in Fig. 3(a).

We plot  $\psi_b$  versus  $s$  in Fig. 3(b) corresponding to not only the configurations shown in Fig. 3(a) but also for the large set of  $\psi_b$  and  $s$  pairs obtained over  $n_T = 10$  trials. The strokes cause the shape of the worm to change over time, introducing fluctuations in the interactions with the boundaries as well as the direction of motion. Nonetheless, the data points are not uniformly scattered, but rather show well defined trends corresponding to when the worm's head is away from a corner or near the corner. Because of the four fold rotational symmetry of the chamber, the distributions repeat after each  $l$ . Further, the points in the upper and lower half denote counterclockwise and clockwise motion along the four sides of the chamber, respectively, and are thus related to each other via a  $\pi$ -rotation. The increasing values of  $\psi_b$  starting near the corner where  $s/l = 0$  till the worm reaches the corner at  $s/l = 1$  thus corresponds to the boundary aligning behavior of the worm in this plot. When the worm gets trapped near the corner,  $\psi_b$  fluctuates between  $\psi_b = 0$  and  $\pi/2$  rad, or  $\psi_b = -\pi/2$  rad and 0, depending on whether the worm is moving anticlockwise or clockwise, respectively. Thus the observed cluster of points in the scatter plot represent boundary aligning and trapping behavior along each of the chamber sides, and corners.

We further characterize the boundary interaction by plotting the projection of the head velocity along the boundary  $v_h^{\parallel}$  as a function of  $\sin(\psi_b)$  in Fig. 3(c). While the data shows considerable scatter, the average trend shown by circle markers obtained by bin averaging over a  $0.1 \sin(\psi_b)$  interval can be described by,

$$v_h^{\parallel} = v_h \sin \psi_b, \quad (1)$$

where  $v_h$  is the average speed of worm's head  $v_h$  away from the boundary. The fit to the data yields  $v_h = 1.74 \text{ mm s}^{-1}$ , as compared with  $v_h = 1.72 \pm 0.65 \text{ mm s}^{-1}$  measured in the experiments while the worm is away from the boundary. Thus, we find that the velocity component parallel to the boundary is similar before and after the head comes in contact with the boundary.

### C. Corner Trapping

In addition to the points which fall on the curves corresponding to the worm moving along the boundary away from the corners, a large number of points can be found near the dotted vertical lines around  $s = 0, l, 2l, 3l$ , and  $4l$  in Fig. 3(b). We plot the probability distribution  $P(|\psi_b|)$  in Fig. 3(d), while the worm's head is in the corners. Although close to a Gaussian, systematic deviations can be observed even considering the statistical fluctuations from trial to trial. The body strokes give rise to a broad distribution centered along the perpendicular bisector angle because the worm pushes against the adjacent walls due to its undulatory and peristaltic strokes.

We plot the corner trapping time  $\tau$  distribution  $P(\tau)$  for  $l = 40$  mm in Fig. 3(e) along with their RMS fluctuations from trial to trial. An exponential function with a mean  $\langle \tau \rangle = 22$  s is also plotted for reference where systematic deviations can be observed. To understand these more deeply, we plot the observed escape time  $\tau$  from a corner versus the initial angle  $\psi_{ci}$  when the worm initially enters the corner in Fig. 3(e). No obvious correlations are apparent since a wide range of initial entry angles give rise to the range of observed  $\tau$ .

We develop a kinematic model to describe the observed boundary aligning behavior next, before developing a model which incorporates the worm's body strokes to understand the trapping at the concave corners.

## IV. KINEMATIC MODEL OF BOUNDARY ALIGNMENT

A schematic representation of a worm interacting with a boundary is shown in Fig. 4(a). We approximate the worm as a frictionless rod of length  $l_w$  sliding at a boundary to model the interaction of the worm's head with the

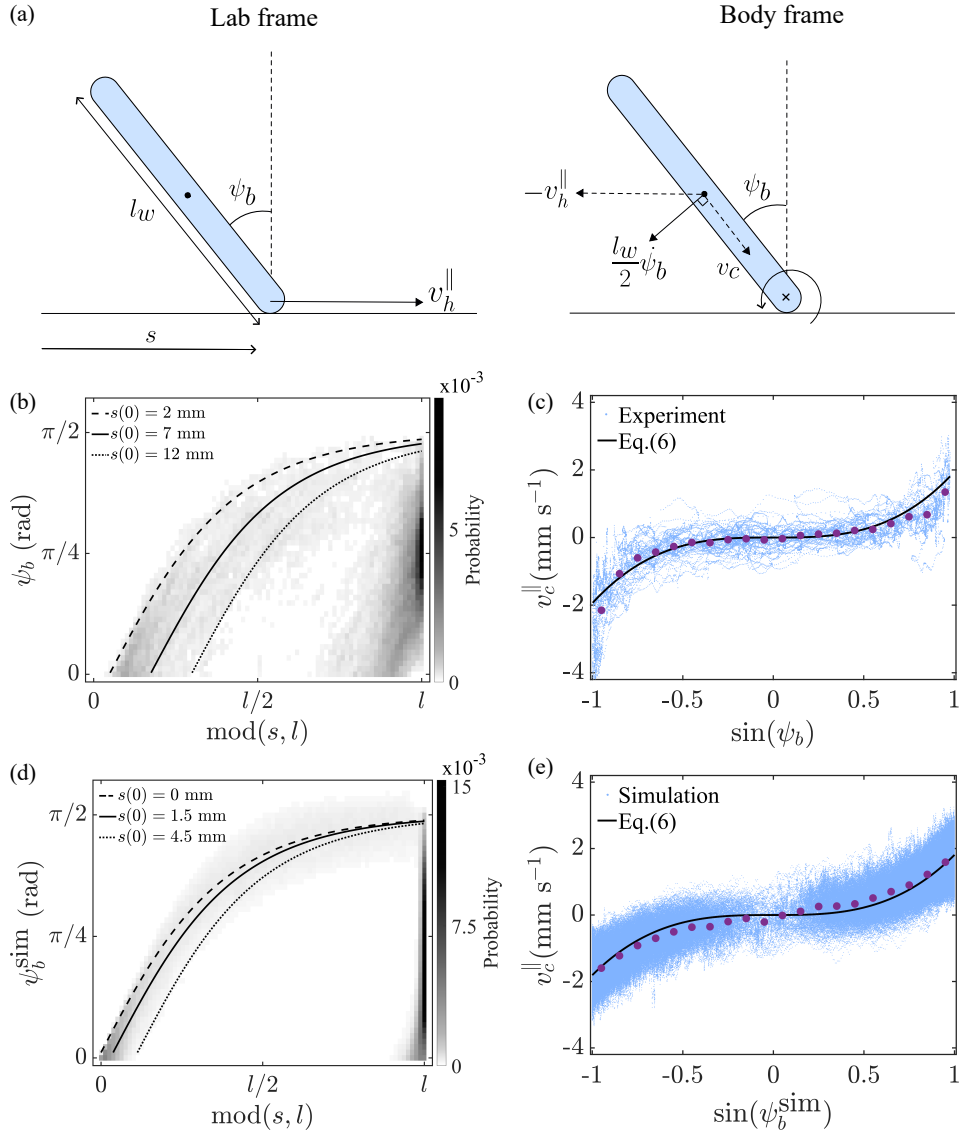


FIG. 4. (a) A rod model of a worm of length  $l_w$  moving near a boundary in the lab and body frame of references. (b) Plot of  $\psi_b$  versus  $\text{mod}(s, l)$ , where the intensity represents the probability of attaining corresponding configuration ( $\text{mod}(s, l)$ ,  $\psi_b$ ). The analytical solution of the kinematic model for  $\psi_b(s)$  with initial orientation  $\psi_b(0) = 0.01$  rad. (c) Worm centroid velocity  $v_c^{\parallel}$  as a function of  $\sin(\psi_b)$ . The data is described by Eq. (5) with  $v_h = 1.94$  mm s $^{-1}$ . (e) The corresponding plot of  $\psi_b$  versus  $\text{mod}(s, l)$  obtained from the active dumbbell model simulations. The analytical solution of the kinematic model for  $\psi_b(s)$  with initial orientation  $\psi_b(0) = 0.035$  rad. (f) The dumbbell-centroid bead velocity  $v_c$  as a function of  $\sin(\psi_b)$  is described by Eq. (5) with  $v_h = 1.81$  mm s $^{-1}$ .

boundary. Then, the angular speed about its center is given by

$$\frac{d\psi_b}{dt} = \frac{v_h^{\parallel} \cos(\psi_b)}{l_w/2}, \quad (2)$$

where  $v_h^{\parallel} = \frac{ds}{dt}$  is the velocity component of the head parallel to the boundary. Substituting Eq. (1) in Eq. (2), we have  $\frac{d\psi_b}{dt} = \frac{v_h \sin(2\psi_b)}{l_w}$ , which upon integration gives,

$$\psi_b = \psi_b(0) \tan^{-1} \left( \exp \left( \frac{2v_h t}{l_w} \right) \right), \quad (3)$$

where  $\psi_b(0)$  is the incident angle of the head when it first comes in contact with a boundary. Solving for  $s$  starting with  $\frac{ds}{dt} = v_h \sin(\psi_b)$ , and using the chain rule  $\frac{ds}{dt} = \frac{ds}{d\psi_b} \frac{d\psi_b}{dt}$ , we get  $\frac{ds}{d\psi_b} = \frac{l_w}{2 \cos(\psi_b)}$ . Integrating, we obtain  $s - s(0) =$

$\frac{l_w}{2} \ln \left( \sqrt{\frac{1+\sin(\psi_b)}{1-\sin(\psi_b)}} \right) - \frac{l_w}{2} \ln \left( \sqrt{\frac{1+\sin(\psi_b(0))}{1-\sin(\psi_b(0))}} \right)$ , where  $\psi_b(0)$  and  $s(0)$  are the initial angle and the initial position of the worm at the boundary, respectively. Rearranging, we find

$$\psi_b = \sin^{-1} \left( \frac{K \exp \left( \frac{4(s-s(0))}{l_w} \right) - 1}{K \exp \left( \frac{4(s-s(0))}{l_w} \right) + 1} \right), \quad (4)$$

with,

$$K = \frac{1 - \sin(\psi_b(0))}{1 + \sin(\psi_b(0))}.$$

We plot Eq. (4) as a blue dashed line in Fig. 3(b), and observe that they correspond to the greatest density of points in Fig. 3(c).

In order to make a more direct comparison, we use the 4-fold rotational symmetry of the chamber, and the clockwise and anti-clockwise symmetry of the worm's motion to map the PDF of finding a worm's head with a particular  $\psi_b$  as a function of the modulus of the distance along the perimeter, i.e.  $\text{mod}(s, l)$ , in Fig. 4(b). We observe two regions which are shaded dark according to the color bar. One corresponds to the motion of the worm along the boundary that are described by Eq. (4), and the other when the worm is trapped in the corners. We plot Eq. (4) with  $s(0) = 7$  mm in Fig. 4(b), and find that  $s(0) = 7$  mm goes through the regions with the highest density when going from one corner to a neighboring corner. Further plotting  $\psi_b(s)$  given by Eq. (4) with  $s(0) = 2$  mm (dashed line) and  $s(0) = 12$  mm (dot line), we find that it roughly bounds most of the data while the worms is away from the corners.

To calculate the speed of the worm along the boundary using the kinematic model, we consider the rod dynamics in the worm reference frame in Fig. 4(a). In this reference frame, the worm rotates about the head as a result of the velocity components at the centroid,  $v_c^{\parallel}$  is the instantaneous centroid velocity according to the lab reference frame, and  $-v_h^{\parallel}$  denotes the negative head speed since we are observing the rod in the head reference frame. On equating velocity components parallel to the rod axis we get,  $-v_h^{\parallel} \sin(\psi_b) + v_c = 0$ . Thus,  $v_c = v_h^{\parallel} \sin(\psi_b) = v_h \sin^2(\psi_b)$ . Then, the component of centroid velocity along the boundary is given by,

$$v_c^{\parallel} = v_c \sin(\psi_b) = v_h \sin^3(\psi_b). \quad (5)$$

We plot  $v_c^{\parallel}$  as a function of  $\sin(\psi_b)$  in Fig. 4(c), along with Eq. (5) using a fitted  $v_h = 1.94$  mm s<sup>-1</sup>.

Thus, the model describes the overall observation that the worm tends to align with the boundary and consequently move faster along the boundary while aligning with the boundary. However, this model is not sufficient to describe the trapping and escape of the worm at the corners. To understand those, we need to go beyond rigid rod dynamics as we discuss next.

## V. ACTIVE ELASTIC DUMBBELL SIMULATIONS

We now develop a minimal active dumbbell model of the worms consisting of two beads connected by a spring inspired by the  $N$ -bead active polymer model [32, 38]. As per our observations in Section III, the worm's head primarily interacts with the boundary, and the orientation of the worm given by the segment joining the head to its centroid relative to the boundary, determines its boundary aligning dynamics. The tail is less active compared to the head, and seldom interacts with the boundaries. Consequently, we use beads corresponding to the head and the centroid of the worm as the minimal model to investigate the dynamics, rather than the head and the tail. A schematic of the bead-spring system and force components are shown in the inset to Fig. 5(a). The time evolution of the beads are described by over-damped Langevin dynamics,

$$\dot{\vec{r}}_i = \frac{1}{\gamma} \sum \vec{F}^i. \quad (6)$$

where  $i = 1, 2$  represents the head and centroid of the worm, respectively, the position vector of the bead  $i$  is  $\vec{r}_i$ ,  $\vec{F}^i$  is the total force acting on the bead  $i$  at time  $t$ ,  $\gamma$  is the viscosity of the medium.

The total force acting on the beads are a result of several components,

$$\vec{F}^i = \vec{F}_s^i + \vec{F}_p^i + \vec{F}_f^i + \vec{F}_n^i + \vec{F}_b^i, \quad (7)$$

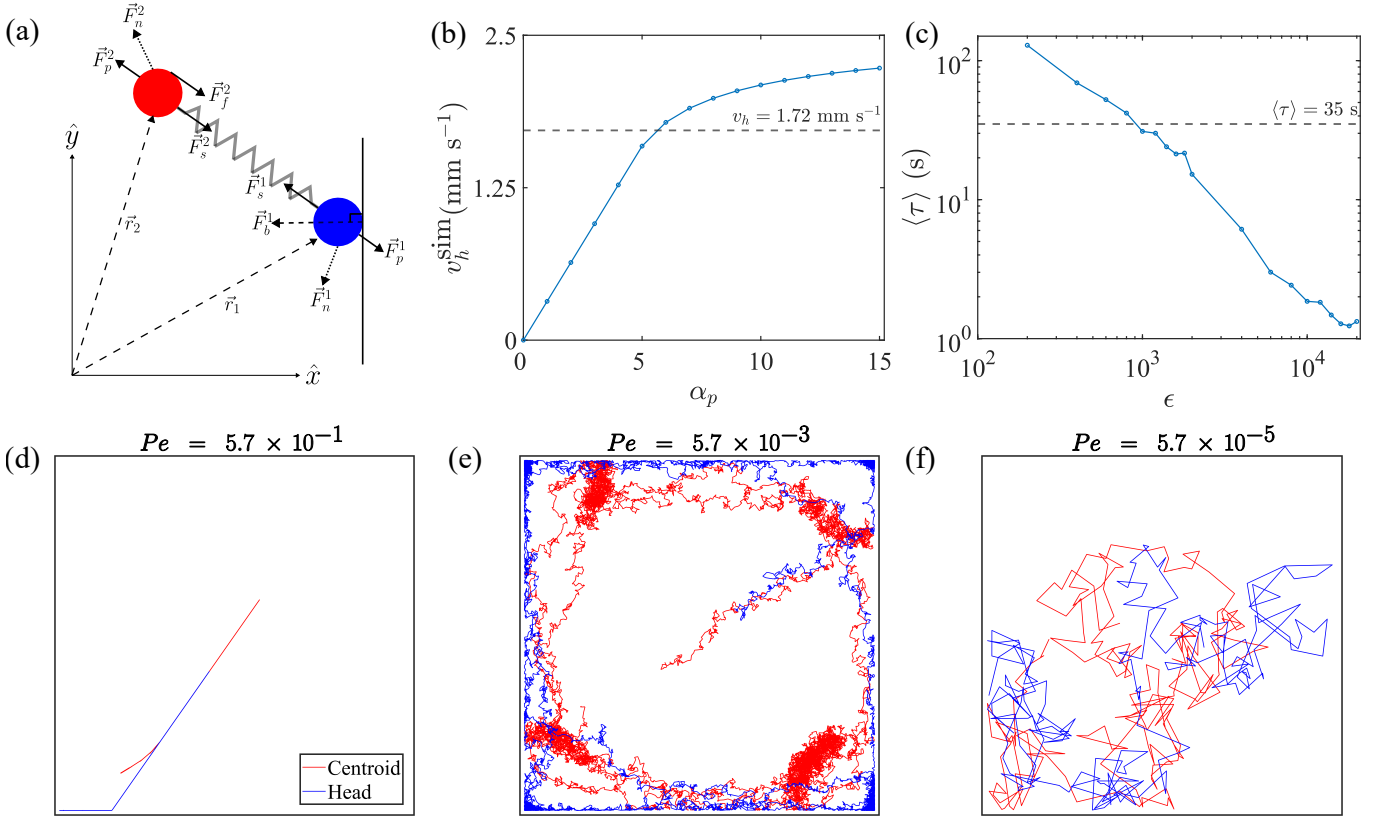


FIG. 5. (a) Schematic of the active elastic dumbbell model. (b) The mean speed of the dumbbell head  $v_h^{\text{sim}}$  increases and then saturates to constant value with  $\alpha_p$ . The dashed line represents the worm's head speed  $v_h$ , away from the boundary. (c) The mean escape time from a corner decreases with  $\epsilon$ . We find  $\epsilon = 8 \times 10^2$  in the simulations correspond to those in observed in the experiments. (d-f) The trajectories of the dumbbell in a square confinement corresponding to different values of  $Pe = \alpha_p/\epsilon$  represents 3 possible dynamical regimes. (d) The dumbbell exhibits boundary following and aligning behavior until it gets permanently trapped in a corner. (e) The dumbbell exhibits dynamical trapping at corners along with boundary following and aligning behavior. This regime qualitatively corresponds to the experimental observations with *L. variegatus*. (f) The dumbbell does not exhibit any boundary aligning and corner trapping behavior due to high fluctuations.

where  $\vec{F}_s^i$  is the spring force between the beads,  $\vec{F}_p^i$  is the propulsion force along the body,  $\vec{F}_f^i$  is the friction force along the body,  $\vec{F}_n^i$  a noise term which captures fluctuations in propulsion in all directions, and  $\vec{F}_b^i$  is the force exerted by the boundary when the beads come in contact.

The force acting on the beads as a result of the stretching/compression of the spring is given by

$$\vec{F}_s^1 = -k(|\vec{r}_1 - \vec{r}_2| - \sigma)\hat{r}_{21} \quad ; \quad \vec{F}_s^2 = -\vec{F}_s^1, \quad (8)$$

where  $k$  is the spring constant,  $\hat{r}_{21}$  is the unit vector along the line joining the centroid to the head, and  $\sigma$  is the equilibrium length of the spring which is chosen equal to  $l_w/2$ .

To capture the propulsion of the worm [29], we implement  $\vec{F}_p^i$  as a sinusoidal force term, acting on each bead along  $\hat{r}_{21}$  as follows:

$$\vec{F}_p^1 = \alpha_p \sin(\omega_p t) \hat{r}_{21} \quad ; \quad \vec{F}_p^2 = -\vec{F}_p^1, \quad (9)$$

where  $\alpha_p$  is the propulsion force amplitude and  $\omega_p = 5 \text{ rad s}^{-1}$  is the fastest body stroke frequency (see SI [37]).

We implement a directional friction term on both beads [39] by setting its magnitude to zero when  $\vec{F}_p^i$  acts along the body orientation  $\hat{r}_{21}$  and non-zero when  $\vec{F}_p^i$  acts opposite to the body orientation  $\hat{r}_{21}$  giving rise to anchoring and forward motion [29]. The magnitude of friction is assumed to increase linearly with  $|\vec{F}_p^i|$  and then become constant



for  $|\vec{F}_p| > F_f^{\max}$ , i.e.

$$\vec{F}_f^i = \begin{cases} |\vec{F}_p^i \cdot \hat{r}_{21}|, & \text{if } \hat{F}_p^i \cdot \hat{r}_{21} < 0, |\vec{F}_p^i| < F_f^{\max}, \\ F_f^{\max}, & \text{if } \hat{F}_p^i \cdot \hat{r}_{21} < 0, |\vec{F}_p^i| \geq F_f^{\max}, \\ 0, & \text{if } \hat{F}_p^i \cdot \hat{r}_{21} \geq 0. \end{cases} \quad (10)$$

To account for the observed anharmonic transverse and body stroke motion, we introduce a noise term,

$$\vec{F}_n^i = \epsilon \eta(t), \quad \text{where } i = 1, 2. \quad (11)$$

We obtain  $\eta(x)$  by drawing a number  $x$  from a standard normal distribution with a mean 0 and a standard deviation 1, i.e,  $\eta(x) = (1/\sqrt{2\pi}) \exp(-x^2/2)$ . Thus,  $\epsilon$  controls the deviation of the worm from a linear path.

The chamber confinement is implemented such that if either of the beads goes outside the confinement, the boundary force  $\vec{F}_b^i$  is such that the normal force pointing outside the confinement is zero. We solve the equations of the motion to obtain the position coordinates of the beads using the method of finite difference. We set the confinement length  $l_{\text{sim}} = 40$  to correspond to those in the experiments. The natural spring length  $\sigma$  connecting two beads is then chosen such that  $\sigma \approx l_w/2 = 10$ , and we set spring coefficient  $k = 1.5$  to reduce the number of parameters. We set the simulation time step  $dt = 10^{-6}$  to resolve the collision with the boundary with sufficient resolution. An individual simulation trial is run for  $t_{\text{sim}} = 1800$  to match the duration of one experiment  $t = 1800$  s.

We introduce a Péclet number  $Pe = \alpha_p/\epsilon$  in analogy with transport phenomena as a measure of the ratio of advection rate to diffusion rate [40]. Then, one may expect the worm to move linearly with limited diffusion and change in orientation as it moves forward for large  $Pe$ . Whereas, the worm may be expected to be more diffusive and change orientation considerably while moving forward for small  $Pe$ . We first perform simulations turning off diffusion, and varying  $\alpha_p$  to obtain the speed of the active dumbbell as a function of distance away from a boundary. Plotting the speed of bead 1 versus  $\alpha_p$  in Fig. 5(b), we observe it increases linearly before beginning to saturate. Comparing with the observed speed  $v_h$  in the experiments, we find  $\alpha_p = 5.7$ . Next, we vary  $\epsilon$  and obtain the mean time to escape a corner  $\tau$  in the simulations and plot it in Fig. 5(c). Then, comparing with the measured value, we find  $\epsilon \approx 8 \times 10^2$ , which then give  $Pe = 7.13 \times 10^{-3}$ .

Figure 5(d-f) shows examples of trajectories corresponding to the head and the centroid of the simulated worm obtained by varying  $\epsilon$ , and consequently  $Pe$ . When the model worm is released at the chamber center with a randomly chosen orientation, it moves forward with increasing change in orientation with decreasing  $Pe$  before encountering the chamber boundary. When the worm encounters a boundary, it turns to align along the boundary, and then gets trapped in a corner for large  $Pe$ . When  $Pe$  corresponding to the calibrated value of  $Pe = 7.13 \times 10^{-3}$  is used, we find that the dumbbell model diffuses as it moves from the center, and turns to align with the boundary, before getting trapped at the corners. Over time, we then observe that it escapes and moves along the boundary to a neighboring corner where it may again get trapped. When  $Pe$  is increased further, the worm diffuses considerably, follows the boundary only to a limited extent, and moves to the chamber center as opposed to staying close to the boundary. Thus,  $Pe$  has a drastic effect on the location of the dumbbell in the chamber over time. Comparing with the typical behavior shown by a California blackworm illustrated in Fig. 2(a), one can note that the intermediate  $Pe = 7.13 \times 10^{-3}$  resembles the observed behavior in the actual worms.

## VI. MODEL COMPARISONS

### A. Boundary alignment

We perform 140 simulation trials with these tuned parameters to analyze and compare the dumbbell dynamics in the square confinement to understand those observed with the California blackworm. Figure 4(d) shows a plot of  $\psi_b^{\text{sim}}$  versus  $\text{mod}(s, l_{\text{sim}})$  where the intensity denotes the probability of attaining a configuration state  $(\text{mod}(s, l_{\text{sim}}), \psi_b^{\text{sim}})$ . The analytical solution for the kinematic model for boundary alignment, Eq. (4) is superimposed for three different initial conditions. As in the experiments, the elastic dumbbell model of the worm is observed to align along the boundary so that  $\psi_b^{\text{sim}} \approx \pi/2$  as it approaches a corner. If the dumbbell gets trapped at the corner, its body orientation is primarily driven by fluctuations, giving rise to a non-zero probability distribution for  $\text{mod}(s, l_{\text{sim}}) \approx l_{\text{sim}}, \psi_b^{\text{sim}} \in (0, \pi/2)$ , with a highest probability at  $\pi/4$ .

For  $\text{mod}(s, l_{\text{sim}}) \approx l_{\text{sim}}, \psi_b^{\text{sim}} \approx 0$  there is a narrow band which denotes the dumbbell when it is oriented perpendicular to the boundary and slips back into a corner. A similar but wider band is observed in experiment from Fig. 4(d).

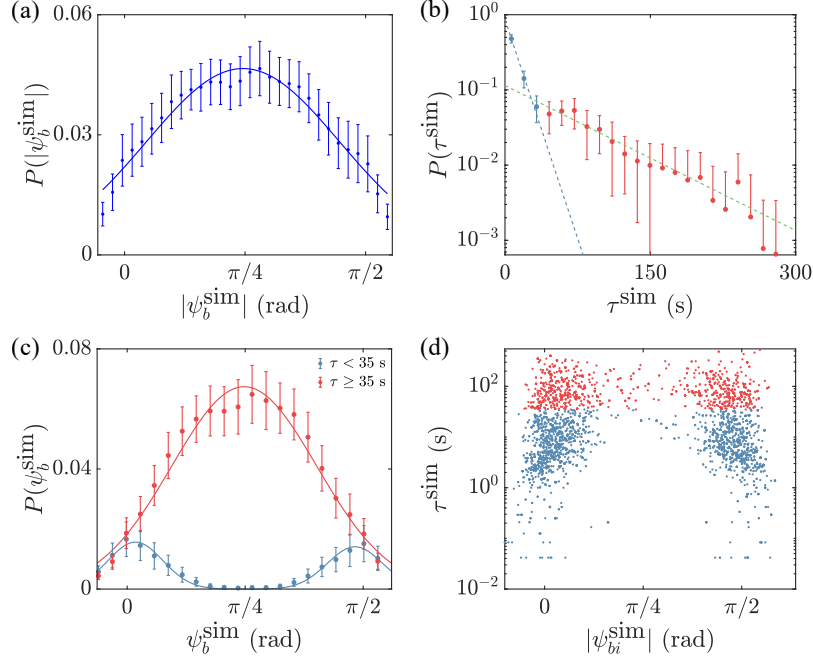


FIG. 6. (a) Probability distribution of body orientation of a dumbbell  $\psi_b^{\text{sim}}$  at a corner. The root mean square deviations of observed values in each trial from the mean is also denoted. A fit to Gaussian with mean  $\psi_b = 0.77$  rad and standard deviation  $0.63$  rad is also shown. (b) Trapping time probability distribution with two exponential fits with mean  $\mu_1 \approx 11$  s, and  $\mu_2 \approx 66$  s are shown. (c) The probability distribution  $|\psi_b^{\text{sim}}|$  corresponding to  $\tau^{\text{sim}} > 35$  s and  $\tau^{\text{sim}} < 35$  s. The  $\psi_b^{\text{sim}}$  do not show significant probability at  $\pi/4$  indicating that they escape right away. (d) The scatter plot of trap time  $\tau^{\text{sim}}$  vs incidence angle  $|\psi_{ci}^{\text{sim}}|$  at a corner.

When trapped, the worm perform undulatory strokes such that its head is incident at a distance comparable to its undulation amplitude, away from the corner. It subsequently converges to the corner while moving along the boundary. In contrast to this mechanism observed in worm, the dumbbell merely fluctuates which results in a narrower band.

In Fig. 4(e), we plot the centroid bead velocity  $v_c^{\parallel}$  vs  $\sin(\psi_b^{\text{sim}})$ , fitted to Eq. (5) with  $v_h^{\text{sim}} = 1.81$  mm s $^{-1}$  which is comparable to  $v_h = 1.94$  mm s $^{-1}$ , obtained from experiments. Thus, we observe all good agreement with the boundary aligning dynamics comparing across with the experimental measurements, active dumbbell simulations, and the analytical results derived from the kinematic model.

## B. Corner trapping and escape

We plot the body orientation probability of a dumbbell at a corner and observe that it is symmetric with a peak at  $\psi_{ci}^{\text{sim}} = \pi/4$  in Fig. 6(a). We further plot the distribution of the trap time observed in the simulations  $\tau^{\text{sim}}$  in Fig. 6(b). We observe that it deviates from a single exponential decay, but may be described as a sum of two exponential.

To explain the orientation distribution in detail, we observe the relationship between the incident angle at a corner  $\psi_{ci}^{\text{sim}}$  and trapping time  $\tau^{\text{sim}}$  for a given trapping event. In Fig. 6(d) we show a semi-log scatter plot of  $\tau^{\text{sim}}$  vs  $\psi_{ci}^{\text{sim}}$ . We observe a symmetric distribution of points about  $\psi_{ci}^{\text{sim}} = \pi/4$ , signifying a similar number of events for encountering a corner from either a clockwise ( $\psi_{ci}^{\text{sim}} = \pi/2$ ) or anti-clockwise ( $\psi_{ci}^{\text{sim}} = 0$ ) direction. There is a high density of points corresponding to  $\psi_{ci}^{\text{sim}} = 0, \pi/2$  as it will be further shown that the dumbbell aligns along the edges before it gets trapped in a corner. For  $\psi_{ci}^{\text{sim}} = 0, \pi/2$  we observe that the density of points decreases with increasing trapping time. Based on this, we classify the trapping events in 2 populations with low ( $\tau < 35$  s), and high trapping time ( $\tau > 35$  s).

In Fig. 6(c) we separately plot the orientation probability for the two populations. For the trapping events with  $\tau < 35$  s the orientation probability is fitted to a two-term normal distribution with  $\mu_1 \approx 0.06$  rad,  $\sigma_1 \approx 0.18$  rad and  $\mu_2 \approx 1.52 \approx \pi/2$  rad,  $\sigma_2 \approx 0.18$  rad. There are two similar normal distributions owing to the symmetry of the confinement. These events correspond to a dumbbell when it is incident at a corner, parallel to an edge and escapes quickly. As clearly seen in the figure, the probability of  $\psi_c^{\text{sim}} = \pi/4$  is almost zero. This implies that the dumbbell

does not get trapped along the angle bisector at the corner. When the dumbbell escapes from a corner it orients itself at  $\psi_c^{\text{sim}} < 0$  and  $\psi_c^{\text{sim}} > \pi/2$ . The orientation probability associated with the population having high trapping time is fitted to a normal distribution with  $\mu \approx 0.78$  rad and  $\sigma \approx 0.48$  rad. These events represent the dumbbell when it orients itself along the angle bisector at a corner. The probability peak is higher compared to the other two populations due to cumulative contributions from events when the dumbbell is incident along  $\psi_{ct}^{\text{sim}} = 0$  and  $\pi/2$ . In this context, the trapping events belonging to this population lose the sense of their initial orientation.

From these insights, we claim that the shape of the orientation probability distribution shown in Fig. 6 (a) is a combined effect of two populations, ones which enter and leave more or less immediately, and others which enter and then leave over random interval of times driven by a stochastic process while the dumbbell orientation fluctuates about the perpendicular bisector at the corner.

## VII. CONCLUSIONS

In summary, we investigated the behavior of *Lumbriculus variegatus* in polygonal chambers with concave and convex corners and contrasted the behavior with that observed in circular chambers. The worm was found near the boundaries with higher probability compared to the central regions of the chamber in all cases. Our observations with a polygonal chamber provide a more subtle view of the interaction of the worm with impenetrable boundaries compared to observations with circular chambers. Enabled by full body tracking of the worm as it moves inside the chamber, we are able to track the boundary aligning dynamics and the role of body strokes which lead to alignment but also random forces at contact which lead to deviations. We find that the worm can be found localized in concave corners, while they do not turn and follow the boundaries at convex corners. Along with the fact that they spontaneously leave the boundaries and corners lead us to postulate that the reason they are found near the boundaries and in the corners is due to purely dynamical consideration, and not due to any shelter seeking mechanism or thigmotaxis.

Then, by performing analysis with a rigid rod model of the worm, we calculate how the nature of the sliding contact during collision determines the observed mean boundary aligning behavior. Then, we develop a minimal active elastic dumbbell model which includes crucial ingredients which lead to forward net motion of the worm due to peristaltic motion, and the fluctuations due to transverse undulations and anharmonic peristaltic motion in an active dumbbell model. We show that this model shows consistent behavior with the boundary aligning dynamics in the experiments as well as the kinematic model. Moreover, it shows the crucial role of fluctuations in enabling the worm to escape dynamical traps as posed by concave corners. We describe all the salient features observed in *Lumbriculus variegatus* including boundary alignment and trap time distributions with models that do not include any thigmotaxis.

Our work shows the crucial role played by boundary curvature in determining localization of an undulating worm which interacts with boundaries only while in contact. Further, it shows that localization at boundaries and corners can arise, even in the absence of long range viscous hydrodynamic interactions, due to purely dynamical reasons as a consequence of the polar nature of their motion and limited rotational diffusion caused by their elongated shapes.

## ACKNOWLEDGMENTS

We thank Animesh Biswas, Vishal Patil, and Simon Bissitt for discussions. We acknowledge the support of the U.S. NSF grant CBET-1805398 and 2401729, and thank Professor Alex Petroff for allowing access and guidance to the Laser-cutter facility in his laboratory.

- 
- [1] Reza Nosrati, Percival J Graham, Qiaozhi Liu, and David Sinton. Predominance of sperm motion in corners. *Scientific reports*, 6(1):26669, 2016.
  - [2] Petr Denissenko, Vasily Kantsler, David J Smith, and Jackson Kirkman-Brown. Human spermatozoa migration in microchannels reveals boundary-following navigation. *Proceedings of the National Academy of Sciences*, 109(21):8007–8010, 2012.
  - [3] Alejandro Guidobaldi, Yogesh Jeyaram, Ivan Berdakin, Victor V Moshchalkov, Carlos Alberto Condat, Verónica Iris Marconi, Laura Giojalas, and Alejandro V Silhanek. Geometrical guidance and trapping transition of human sperm cells. *Physical Review E*, 89(3):032720, 2014.
  - [4] Karl G Götz and Roland Biesinger. Centrophobism in drosophila melanogaster: Ii. physiological approach to search and search control. *Journal of Comparative Physiology A*, 156:329–337, 1985.
  - [5] Morgane Besson and Jean-René Martin. Centrophobism/thigmotaxis, a new role for the mushroom bodies in drosophila. *Journal of neurobiology*, 62(3):386–396, 2005.

- [6] Christopher J. May, Jeffrey C. Schank, Sanjay Joshi, Jonathan Tran, R. J. Taylor, and I-Esha Scott. Rat pups and random robots generate similar self-organized and intentional behavior. *Complexity*, 12(1):53–66, 2006.
- [7] RP Creed and JR Miller. Interpreting animal wall-following behavior. *Experientia*, 46:758–761, 1990.
- [8] Saurabh Sharma, Sheryl Coombs, Paul Patton, and Theresa Burt De Perera. The function of wall-following behaviors in the mexican blind cavefish and a sighted relative, the mexican tetra (*astyanax*). *Journal of Comparative Physiology A*, 195:225–240, 2009.
- [9] Janos Kallai, Tamas Makany, Arpad Csatho, Kazmer Karadi, David Horvath, Beatrix Kovacs-Labadi, Robert Jarai, Lynn Nadel, and Jake W Jacobs. Cognitive and affective aspects of thigmotaxis strategy in humans. *Behavioral neuroscience*, 121(1):21, 2007.
- [10] Nora Walz, Andreas Mühlberger, and Paul Pauli. A human open field test reveals thigmotaxis related to agoraphobic fear. *Biological Psychiatry*, 80(5):390–397, 2016.
- [11] Xue Ying Zhang, Marta Diaz-delCastillo, Lingsi Kong, Natasha Daniels, William MacIntosh-Smith, Aya Abdallah, Dominik Domanski, Denis Sofrenovic, Tsz Pui (Skel) Yeung, Diego Valiente, Jan Vollert, Emily Sena, Andrew S. Rice, and Nadia Soliman. A systematic review and meta-analysis of thigmotactic behaviour in the open field test in rodent models associated with persistent pain. *PLOS ONE*, 18(9):1–44, 09 2023.
- [12] Arshad Kudrolli, Geoffroy Lumay, Dmitri Volfson, and Lev S Tsimring. Swarming and swirling in self-propelled polar granular rods. *Physical review letters*, 100(5):058001, 2008.
- [13] Guanglai Li and Jay X. Tang. Accumulation of microswimmers near a surface mediated by collision and rotational brownian motion. *Phys. Rev. Lett.*, 103:078101, Aug 2009.
- [14] Paul D Frymier, Roseanne M Ford, Howard C Berg, and Peter T Cummings. Three-dimensional tracking of motile bacteria near a solid planar surface. *Proceedings of the National Academy of Sciences*, 92(13):6195–6199, 1995.
- [15] Allison P Berke, Linda Turner, Howard C Berg, and Eric Lauga. Hydrodynamic attraction of swimming microorganisms by surfaces. *Physical Review Letters*, 101(3):038102, 2008.
- [16] Eric Lauga and Thomas R Powers. The hydrodynamics of swimming microorganisms. *Reports on Progress in Physics*, 72(9):096601, aug 2009.
- [17] Vasily Kantsler, Jörn Dunkel, Marco Polin, and Raymond E Goldstein. Ciliary contact interactions dominate surface scattering of swimming eukaryotes. *Proceedings of the National Academy of Sciences*, 110(4):1187–1192, 2013.
- [18] Koen Schakenraad, Linda Ravazzano, Niladri Sarkar, Joeri A. J. Wondergem, Roeland M. H. Merks, and Luca Giomi. Topotaxis of active brownian particles. *Phys. Rev. E*, 101:032602, Mar 2020.
- [19] Zeinab Sadjadi and Heiko Rieger. Topotaxis of active particles across long distances by sliding along obstacles. *Phys. Rev. Res.*, 6:013178, Feb 2024.
- [20] Sunghwan Jung. *Caenorhabditis elegans* swimming in a saturated particulate system. *Physics of Fluids*, 22(3):031903, 2010.
- [21] Tapomoy Bhattacharjee and Sujit S Datta. Bacterial hopping and trapping in porous media. *Nature Communications*, 10(1):1–9, 2019.
- [22] Blair A. Jenkins and Ellen A. Lumpkin. Developing a sense of touch. *Development*, 144(22):4078–4090, 11 2017.
- [23] CD Drewes and RO Brinkhurst. Giant nerve fibers and rapid escape reflexes in newly hatched aquatic oligochaetes, *lumbriculus variegatus* (family lumbriculidae). *Invertebrate reproduction & development*, 17(2):91–95, 1990.
- [24] Nalena M Lesiuk and Charles D Drewes. Autotomy reflex in a freshwater oligochaete, *lumbriculus variegatus* (clitellata: Lumbriculidae). *Hydrobiologia*, 406:253–261, 1999.
- [25] Charles D Drewes and Charles R Fournier. Morphallaxis in an aquatic oligochaete, *lumbriculus variegatus*: reorganization of escape reflexes in regenerating body fragments. *Developmental Biology*, 138(1):94–103, 1990.
- [26] Charles Drewes and Kacia Cain. As the worm turns: Locomotion in a freshwater oligochaete worm. *The American Biology Teacher*, 61:438–442, 1999.
- [27] Charles D Drewes. Helical swimming and body reversal behaviors in *lumbriculus variegatus* (annelida: Clitellata: Lumbriculidae). *Hydrobiologia*, 406:263–269, 1999.
- [28] CD Drewes and CR Fournier. Hindsight and rapid escape in a freshwater oligochaete. *The Biological Bulletin*, 177(3):363–371, 1989.
- [29] Arshad Kudrolli and Bernny Ramirez. Burrowing dynamics of aquatic worms in soft sediments. *Proceedings of the National Academy of Sciences*, 116(51):25569–25574, 2019.
- [30] Animesh Biswas and Arshad Kudrolli. Escape dynamics of confined undulating worms. *Soft Matter*, 19:4376–4384, 2023.
- [31] Vishal P Patil, Harry Tuazon, Emily Kaufman, Tuhin Chakraborty, David Qin, Jörn Dunkel, and M Saad Bhamla. Ultrafast reversible self-assembly of living tangled matter. *Science*, 380(6643):392–398, 2023.
- [32] Chantal Nguyen, Yasemin Ozkan-Aydin, Harry Tuazon, Daniel I Goldman, M Saad Bhamla, and Orit Peleg. Emergent collective locomotion in an active polymer model of entangled worm blobs. *Frontiers in Physics*, 9:734499, 2021.
- [33] A Deblais, AC Maggs, D Bonn, and S Woutersen. Phase separation by entanglement of active polymerlike worms. *Physical Review Letters*, 124(20):208006, 2020.
- [34] Antoine Deblais, Sander Woutersen, and Daniel Bonn. Rheology of entangled active polymer-like *t. tubifex* worms. *Physical Review Letters*, 124(18):188002, 2020.
- [35] Yasemin Ozkan-Aydin, Daniel I Goldman, and M Saad Bhamla. Collective dynamics in entangled worm and robot blobs. *Proceedings of the National Academy of Sciences*, 118(6):e2010542118, 2021.
- [36] Lara Zirbes, Yves Brostaux, Mark Mescher, Maxime Jason, Eric Haubruge, and Jean-Louis Deneubourg. Self-assembly and quorum in the earthworm *isenia fetida* (oligochaete, lumbriculidae). *PLoS one*, 7(3):e32564, 2012.
- [37] See supplemental material at [url will be inserted by publisher] for further information on methods, movies and analysis.

- [38] Roland G. Winkler and Gerhard Gompper. The physics of active polymers and filaments. The Journal of Chemical Physics, 153(4):040901, 07 2020.
- [39] Yoshimi Tanaka, Kentaro Ito, Toshiyuki Nakagaki, and Ryo Kobayashi. Mechanics of peristaltic locomotion and role of anchoring. Journal of the Royal Society Interface, 9(67):222–233, 2012.
- [40] Praveen Kumar and Rajarshi Chakrabarti. Escape dynamics of a self-propelled nanorod from circular confinements with narrow openings. Soft Matter, 19:6743–6753, 2023.